RSC Advances

PAPER

View Article Online
View Journal | View Issue



Cite this: *RSC Adv.*, 2020, **10**, 21375

# Chemically anchored two-dimensional-$SiO_x$/zero-dimensional-$MoO_2$ nanocomposites for high-capacity lithium storage materials†

Soohwan Kim, Hyundong Yoo and Hansu Kim *

Received 17th March 2020
Accepted 17th May 2020

DOI: 10.1039/d0ra02462g

rsc.li/rsc-advances

Silicon oxides are promising alternatives for graphite anodes in lithium-ion batteries. $SiO_x$ nanosheets exhibit favorable anodic performances, including outstanding capacity retention and dimensional stability, due to their unique two-dimensional (2D) microstructures, but suffer from low specific capacity and poor initial coulombic efficiency. Here we demonstrate that chemically anchoring of molybdenum dioxide ($MoO_2$) nanoparticles on the surface of 2D-$SiO_x$ nanosheets *via* a Mo–O–Si bond boosts both the reversible capacity and initial coloumbic efficiency without sacrificing the useful properties of 2D-$SiO_x$ nanosheets. The enhancements can be attributed to the introduction of a zero-dimensional $MoO_2$ nano-object, which offers abnormal storage sites for lithium. The proposed nano-architecturing shows how we can maximize the advantages of 2D nanomaterials for energy storage applications.

## Introduction

Lithium-ion batteries (LIBs) are used in diverse application such as portable electronic devices, electric vehicles, and energy storage systems[1–3] due to their relatively high energy and power densities.[4,5] Growing demands for batteries in various applications are driving efforts to advance battery performance.[6,7] However, state-of-the-art LIB technology based on graphite anodes appears to have reached its limit,[8,9] and numerous materials have been suggested for alternative anode materials.[10–13] Silicon-based materials offer a high theoretical capacity (3580 mA h $g^{-1}$, $Li_{3.75}Si$) and relatively low operating potential (~0.4 V *vs.* $Li/Li^+$),[14–16] but several constraints must be addressed before such materials can be used in practical applications. For example, volume changes of approximately 300% during lithiation and delithiation can undermine cycling performance.[16–18] To overcome this drawback, various Si-based anode materials, such as $SiO_x$-based composites, Si-carbon nanocomposites, and Si-transition metal alloys, have been proposed to minimize the mechanical strain induced by severe volume changes.[19–23]

Recently, we developed two-dimensional (2D) $SiO_x$ nanosheets for use as anode materials in LIBs through a scalable and cost-effective sol–gel process.[24] The 2D-$SiO_x$ nanosheets moderated volume expansion, enhanced cycling performance, and suppressed volume changes by taking advantage of the unique nano-architecture of 2D nanosheets. First, the absolute volume changes in thin-layered $SiO_x$ (thickness of approximately 8 nm) are much smaller than those of other Si-based anode materials. Second, randomly stacked 2D-$SiO_x$ nanosheet electrodes incorporate abundant free spaces that can accommodate volume changes in $SiO_x$.[24]

Despite such advantages, several technical issues remained to be resolved, including a low reversible capacity less than 600 mA h $g^{-1}$ and a poor initial coulombic efficiency of approximately 30%. To address these problems, we designed nanocomposites of 2D-$SiO_x$ nanosheets with zero-dimensional (0D) molybdenum dioxide ($MoO_2$) nanoparticles because devising complex with 0D nanomaterials would be an alternative for complementing imperfection of 2D nanomaterials.[25,26] We anticipated that such nanosheets would not require sacrificing the advantages of 2D-$SiO_x$ nanosheets because unique electrochemical properties of nanostructured $MoO_2$. Nanostructured $MoO_2$ has a lithium storage capacity far beyond its theoretical capacity based on conversion reactions with lithium due to its abnormal lithium storage reaction mechanism, as well as has a highly stable cycling performance over prolonged cycles.[27–29] We placed 0D-$MoO_2$ nanoparticles on the surface of 2D-$SiO_x$ nanosheets using simple carbothermic reduction of $MoO_3$ with urea. In the proposed 2D-$SiO_x$/0D-$MoO_2$ nanocomposites, 0D-$MoO_2$ nanoparticles bonded tightly to 2D-$SiO_x$ nanosheets *via* a Mo–O–Si bond, providing highly stable capacity retention upon repeated charge–discharge cycles. The resulting synergistic effect through creating chemical bonds with 0D-$MoO_2$ nanoparticles without sacrificing the unique properties of $SiO_x$-based anodes, would be another successful example that show how 2D nanomaterial overcomes its drawbacks with maintaining its unique properties for electrochemical energy storage applications.

*Department of Energy Engineering, Hanyang University, 222 Wangsimni-ro, Seongdong-gu, Seoul, 04763, Republic of Korea. E-mail: khansu@hanyang.ac.kr*

† Electronic supplementary information (ESI) available: FESEM images, and galvanostatic charge–discharge curves. See DOI: 10.1039/d0ra02462g

# Experimental

### Material preparation

2D-$SiO_x$ nanosheets and $MoO_3$ were prepared by our previously reported synthetic route.[24,28] 2D-$SiO_x$ nanosheets were prepared by interfacial sol–gel reaction of trichlorosilane (Tokyo Chemical Industry, > 98%) at the interface between water and air. Trichlorosilane (1.5 mL) was centered in the middle of a glass cylinder (diameter: 14 cm) filled with deionized water (200 mL) at room temperature. After 10 min, shredded-sheet-like hydrogen silsesquioxane (HSQ, $HSiO_{1.5}$) was obtained at the surface of the deionized water. The particles were filtered and washed several times with deionized water to remove the residual acid. Filtered powders were collected and dried in a convection oven at 80 °C until the moisture was completely evaporated. The obtained HSQ was heat-treated at 1000 °C for 1 h under a 4% $H_2$/Ar atmosphere at a heating rate of 20 °C $min^{-1}$ and a flow rate of 0.5 L $min^{-1}$ to generate 2D-$SiO_x$ nanosheets. $MoO_3$ was prepared from the precipitation of an ammonium molybdate tetrahydrate (Sigma-Aldrich, 81.0–83.0% $MoO_3$ basis) aqueous solution (0.05 M, 100 mL) using nitric acid solution (3 mL) (Sigma-Aldrich, 70%). The solution was stirred at room temperature for 3 h and its precipitates were filtered and washed several times with deionized water to remove the residual acid. Filtered $MoO_3$ powders were collected and dried in a convection oven at 80 °C. 2D-$SiO_x$/0D-$MoO_2$ nanocomposites were synthesized by simple mixing of starting materials and carbothermic reduction of the mixture with urea. First, the obtained 2D-$SiO_x$ nanosheets were sonicated for 20 min in ethanol (30 mL) (Daejung Chemicals & Metals, 99.9%) and the obtained $MoO_3$ was stirred for 1 h in ethanol (15 mL) to obtain well-dispersed particles. Then, dispersed 2D-$SiO_x$ nanosheets and $MoO_3$ particles were mixed together and stirred for 1 h at room temperature. After 1 h, the mixture was stirred and heated at 70 °C to evaporate the ethanol, and the obtained powders were then mixed with urea (Sigma-Aldrich, > 98%) ($MoO_3$ : urea = 2 : 1, by weight) for carbothermic reduction of $MoO_3$. Finally, 2D-$SiO_x$/0D-$MoO_2$ nanocomposites were obtained after heat treatment of the urea-mixed powders at 500 °C for 2 h under an $N_2$ atmosphere at a heating rate of 10 °C $min^{-1}$.

### Structural characterization

The surface morphology and microstructures of the particles were characterized by field emission scanning electron microscope (FEI Verios G4 UC) and high-resolution transmission electron microscope (JEOL JEM-2100F). The microstructures of the samples were further identified by an X-ray diffractometer (Rigaku SmartLab) equipped with a 3D pixel semiconductor detector using Cu-K$\alpha$ radiation. A Raman spectrometer (Horiba Jobin-Yvon LabRam ARAMIS) with an Ar-ion laser at a wavelength of 514 nm was employed to identify the obtained 2D/0D nanocomposites. The chemical bonds of the samples were further investigated using an FTIR spectrophotometer (Thermo Scientific Nicolet 6700).

### Electrochemical measurements

Electrochemical tests were performed using CR2032 coin-type cells with a lithium metal counter electrode. The working electrodes were prepared by coating slurries on 10 μm-thick copper foil with a mass loading of 1.0 mg $cm^{-2}$. The slurries, containing 2D-$SiO_x$ nanosheets and 2D-$SiO_x$/0D-$MoO_2$ nanocomposites as the active materials were made by mixing the active material (70 wt%), Super-P as a conductive agent (10 wt%), and poly(acrylic acid) (PAA) as a binder (20 wt%) in deionized water. The slurry-coated electrodes were dried at 120 °C for 2 h in a vacuum oven. The coin-type cells were assembled in an Ar-filled glove box using a polyethylene membrane (Celgard 2400 membrane) as a separator and 1 M $LiPF_6$ dissolved in a mixed solvent of ethylene carbonate and ethyl methyl carbonate (3 : 7 v/v) with additives of fluoroethylene carbonate (2 wt%) (Panax Etec Co., Ltd.) as an electrolyte. The galvanostatic charge/discharge measurement was carried out using a battery-testing system (BaSyTec Cell Test System) at current densities of 200 mA $g^{-1}$ at a voltage range of 0.005 to 3.0 V *versus* $Li/Li^+$. Charging (lithium insertion) was performed in a constant current–constant voltage mode and discharging was performed with in a constant-current mode. The structural changes of the discharged and charged 2D-$SiO_x$/0D-$MoO_2$ nanocomposites electrodes were analysed by *ex situ* XRD analysis during cycling.

# Results and discussion

Fig. 1a illustrates a synthetic route for the proposed 2D-$SiO_x$/0D-$MoO_2$ nanocomposites, in which 0D-$MoO_2$ nanoparticles fabricated by carbothermic reduction of $MoO_3$ particles are chemically anchored to the surface of 2D-$SiO_x$ nanosheets. Urea performed a dual role of reducing agent and dispersant for reduction of $MoO_3$ to $MoO_2$.[30] Fig. 1b–e shows transmission electron microscopy (TEM) images of the 2D-$SiO_x$ nanosheets and 2D-$SiO_x$/0D-$MoO_2$ nanocomposites with different amounts of $MoO_2$ (20, 30, and 40 wt%). As previously reported,[24] bare 2D-$SiO_x$ nanosheets have a 2D sheet-like morphology (width: ~20 μm, thickness: ~8 nm) with a smooth surface (Fig. 1b). Due to very small sizes of 0D-$MoO_2$ nanoparticles, it was hard to observe them using a scanning electron microscopy (SEM) images (Fig. S1†), but TEM images of 0D-$MoO_2$ nanoparticles reveal that $MoO_2$ nanoparticles with the diameter of about 10 nm were formed on the 2D-$SiO_x$ nanosheets (Fig. 1c–e). The size and amounts of the nanoparticles increased as $MoO_2$ was added. High-resolution TEM images with corresponding fast Fourier transformation (FFT) patterns confirmed the formation of 0D-$MoO_2$ nanoparticles from the d-spacing values for the (110) plane of $MoO_2$, with sizes ranging between 5 nm and 20 nm (Fig. 1f–i).

X-ray diffraction (XRD) patterns confirmed the formation of $MoO_2$ on the surface of the 2D-$SiO_x$ nanosheets (Fig. 2a). All XRD patterns showed a broad Bragg peak at $2\theta = 21.8°$, which is a general characteristic of amorphous Si suboxides.[31–34] Other Bragg peaks appeared in the XRD patterns of 2D-$SiO_x$/0D-$MoO_2$ nanocomposites at $2\theta$ = 26.0°, 37.0°, 53.5°, 60.2°, 66.6°, and

 

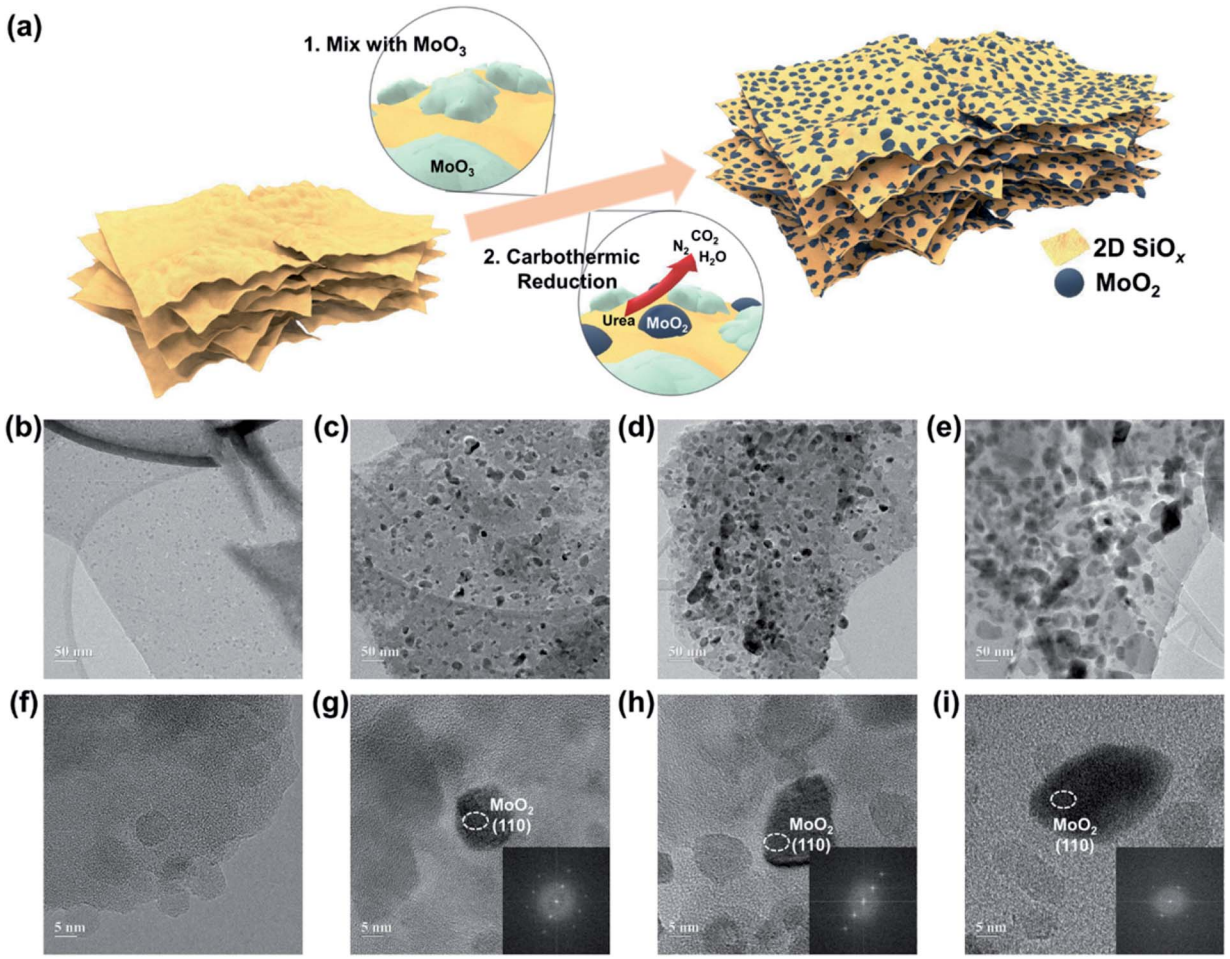


Fig. 1 (a) Schematic illustration of the synthetic route for the proposed 2D-$SiO_x$/0D-$MoO_2$ nanocomposites. (b–e) TEM images and (f–i) HRTEM images with FFT patterns of the 2D-$SiO_x$ nanosheets and 2D-$SiO_x$/0D-$MoO_2$ nanocomposites; (b and f) bare 2D-$SiO_x$ nanosheets, (c and g) 20 wt%, (d and h) 30 wt%, and (e and i) 40 wt% of $MoO_2$ contained 2D-$SiO_x$/0D-$MoO_2$ nanocomposites.

78.7°, which corresponded to $MoO_2$.[35,36] The strongest peak in the XRD patterns of 2D-$SiO_x$/0D-$MoO_2$ nanocomposites at $2\theta = 26.0°$ corresponded to the (110) plane of $MoO_2$, which matched the aforementioned FFT pattern analysis on the 2D-$SiO_x$/0D-$MoO_2$ nanocomposites. Fig. 2b shows Raman spectra of the 2D-$SiO_x$ nanosheets and 2D-$SiO_x$/0D-$MoO_2$ nanocomposites, with the spectra for $MoO_2$ particles included as a reference. 2D-$SiO_x$/0D-$MoO_2$ nanocomposites showed typical bands for $MoO_2$,[37]

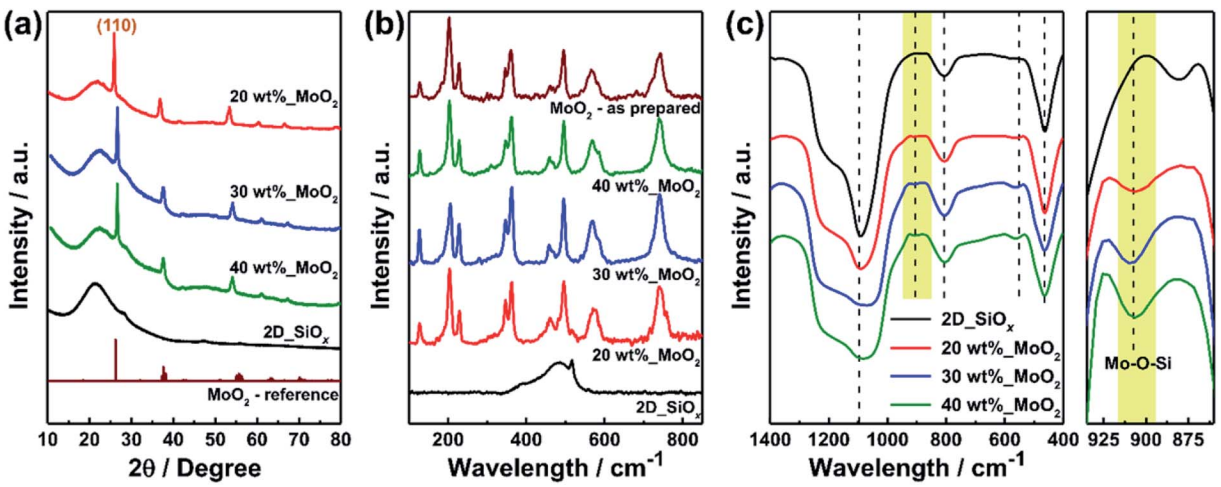


Fig. 2 (a) XRD patterns, (b) Raman spectra, and (c) FTIR spectra for the 2D-$SiO_x$/0D-$MoO_2$ nanocomposites with the different amounts of $MoO_2$.

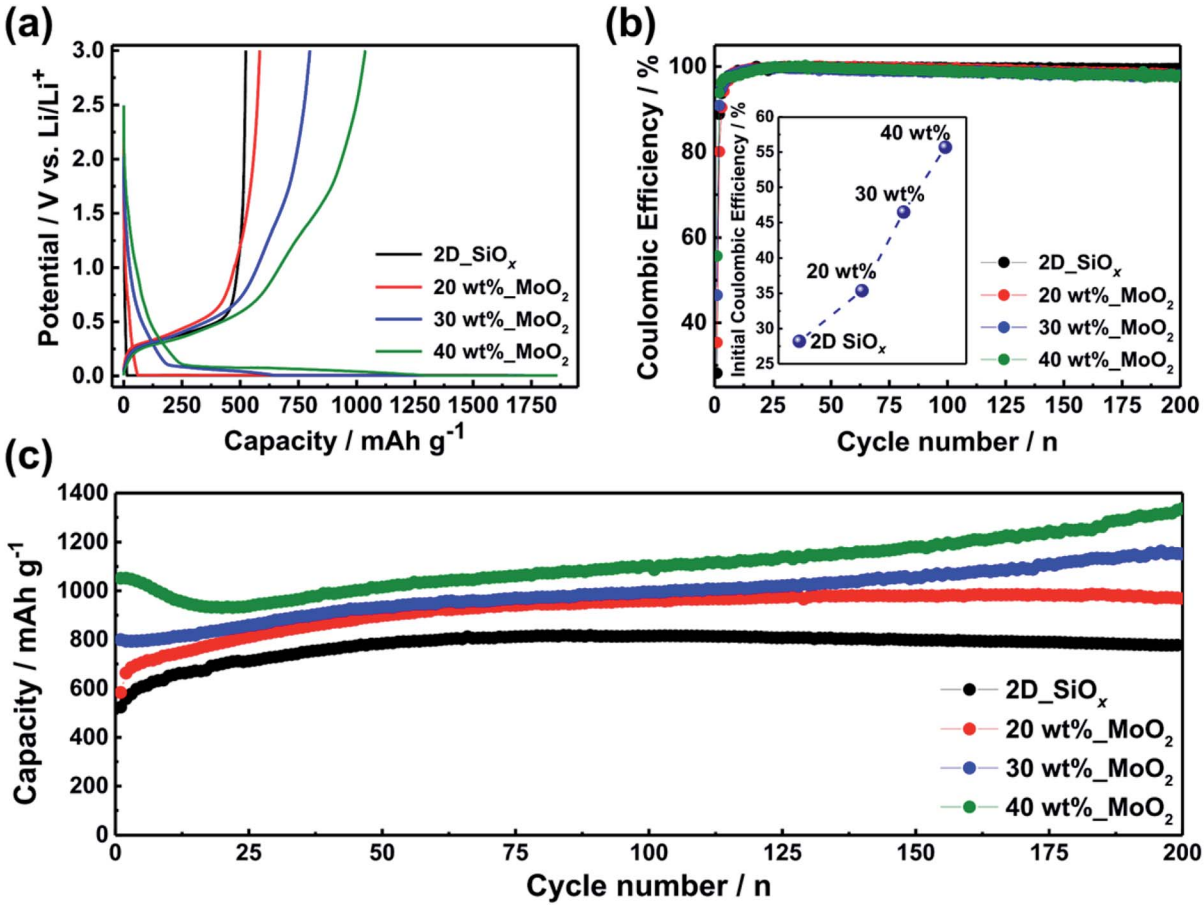


Fig. 3 Electrochemical performance of the 2D-$SiO_x$/0D-$MoO_2$ nanocomposites with the different amount of $MoO_2$. (a) Galvanostatic voltage profiles in the voltage range of 0.005–3.0 V *versus* $Li/Li^+$ at a constant current density of 0.2C (200 mA $g^{-1}$) for the first cycle, (b) coulombic efficiency in the first cycle and for 200 cycles, and (c) cycling performance at a constant current density of 0.2C (200 mA $g^{-1}$) for 200 cycles.

while Raman spectra for the 2D-$SiO_x$ nanosheets only showed a single Raman band near 480 $cm^{-1}$, corresponding to amorphous Si,[38] which was commonly observed as non-stoichiometric $SiO_x$. No band for amorphous Si was observed for the 2D-$SiO_x$/0D-$MoO_2$ nanocomposites because the intensity of the Raman bands for $MoO_2$ were much stronger than that of amorphous Si and they overlapped the $MoO_2$ bands.

To identify specific structures of the 2D-$SiO_x$/0D-$MoO_2$ nanocomposites, it was necessary to determine whether chemical bonding occurred in 2D-$SiO_x$ nanosheets and 0D-$MoO_2$ nanoparticles. Fig. 2c shows Fourier transform infrared (FTIR) spectra of the 2D-$SiO_x$ nanosheets and 2D-$SiO_x$/0D-$MoO_2$ nanocomposites. Peaks at 1100, 806, and 470 $cm^{-1}$ in all samples were assigned to asymmetric vibration of Si–O–Si, symmetric stretching vibration of Si–O–Si, and bending vibration of Si–O–Si, respectively,[39–41] from the 2D-$SiO_x$ nanosheets. Mo–O–Si bond and symmetric stretching of Mo–O–Mo near 908 and 560 $cm^{-1}$ were also observed in all 2D-$SiO_x$/0D-$MoO_2$ nanocomposite samples.[42,43] The appearance of a Mo–O–Si bond in the FTIR spectra implies that the 0D-$MoO_2$ nanoparticles were tightly anchored with the 2D-$SiO_x$ nanosheets through chemical bonding, not just placed on the surface of 2D-$SiO_x$ nanosheets.

Voltage profiles of the 2D-$SiO_x$ nanosheets and 2D-$SiO_x$/0D-$MoO_2$ nanocomposites electrodes with different amounts of $MoO_2$ (20, 30, and 40 wt%) for the first cycle are shown in Fig. 3a. The 2D-$SiO_x$ nanosheets electrode delivered an initial reversible capacity of 524.0 mA h $g^{-1}$, while the 2D-$SiO_x$/0D-$MoO_2$ nanocomposites electrodes exhibited higher initial reversible capacities of 584.0 mA h $g^{-1}$ (20 wt%), 799.2 mA h $g^{-1}$ (30 wt%), and 1051.6 mA h $g^{-1}$ (40 wt%). The initial reversible capacities of the 2D-$SiO_x$/0D-$MoO_2$ nanocomposites electrodes increased as the amount of $MoO_2$ increased, eventually doubling that of bare 2D-$SiO_x$ nanosheets electrode. The 2D-$SiO_x$/0D-$MoO_2$ nanocomposites electrodes also showed enhanced initial coulombic efficiencies of 35.4% (20 wt%), 46.5% (30 wt%), and 55.7% (40 wt%) compared with the 2D-$SiO_x$ nanosheets electrode (28.2%) (Fig. 3b). The improved performances can be attributed to the exceptional lithium storage behavior of nanostructured $MoO_2$,[29] which could compensate for the low initial capacity and poor initial coulombic efficiency of the 2D-$SiO_x$ nanosheet electrode.[24] Fig. 3c shows the long-term cycling performance of the 2D-$SiO_x$ nanosheet electrode and 2D-$SiO_x$/0D-$MoO_2$ nanocomposite electrodes at a constant current density of 200 mA h $g^{-1}$ for 200 cycles. All samples exhibited highly stable cycling performances

 

over 200 cycles with stable coulombic efficiencies (Fig. 3b and c). A gradual increase in reversible capacities of all the samples was evident during cycling due to the gradual activation of amorphous $SiO_x$ matrix toward lithium-ion insertion and extraction.[23,24,32,44] A further increase in the reversible capacities of the 2D-$SiO_x$/0D-$MoO_2$ nanocomposites electrodes was also evident. The increase in the capacity of the 2D-$SiO_x$/0D-$MoO_2$ nanocomposites electrodes can be attributed to the activation of $MoO_2$ nanoparticles associated with the unique microstructural evolution of nanostructured $MoO_2$.[45,46] These increasing trends were also observed in charge–discharge curves for selected cycles (Fig. S2†). This cycling performance was due to the favorable microstructures and dimensional stability of the 2D-$SiO_x$ nanosheets as well as the outstanding lithium storage properties of 0D-$MoO_2$ nanoparticles.[24,28,45–47]

Differential capacity plots (DCPs) of the 2D-$SiO_x$/0D-$MoO_2$ nanocomposites electrode upon first discharge within a voltage range of 0.0 to 2.0 V (*vs.* $Li/Li^+$) revealed the aforementioned reaction pathways of the 2D-$SiO_x$/0D-$MoO_2$ nanocomposite electrode (Fig. 4a). Among four different DCPs peaks, the sharp peak of the 2D-$SiO_x$/0D-$MoO_2$ nanocomposite electrodes at 0.32 V corresponded to the delithiation of a-$Li_xSi$.[16,48,49] Three other peaks at 0.47 V, 1.39 V, and 1.70 V reflected the delithiation of $Li_xMoO_2$,[50,51] which also originated from the delithiation reaction of the $MoO_2$ electrode (the brown line in Fig. 4a). The electrochemical reaction process of the 0D-$MoO_2$ nanoparticles anchored on the 2D-$SiO_x$ nanosheets during delithiation helped compensate for the low initial capacity and poor initial coulombic efficiency of the 2D-$SiO_x$ nanosheet electrode.[24] To investigate the improved lithium storage mechanism of the 2D-$SiO_x$/0D-$MoO_2$ nanocomposite electrode, we explored how the crystalline structures of the 2D-$SiO_x$/0D-$MoO_2$ nanocomposites changed during the electrochemical reaction. Fig. 4b shows *ex situ* XRD patterns of the 2D-$SiO_x$/0D-$MoO_2$ nanocomposite electrodes for the first cycle. We found that the Bragg peaks for $MoO_2$ shifted to a lower angle upon lithium insertion due to the phase transition of $MoO_2$ to $Li_{0.98}MoO_2$. We found no Bragg peak corresponding to the metallic Mo or $Li_2O$ phases, which are typical reaction products formed by conversion reaction of $MoO_2$ with lithium ions. This implies that the 2D-$SiO_x$/0D-$MoO_2$ nanocomposites did not follow conventional conversion reactions of $MoO_2$,[52] but reacted instead with lithium ions through another lithium storage mechanism. It is not surprising that nanostructured $MoO_2$ did not follow conventional conversion reactions. Shon *et al.* reported that ordered mesoporous $MoO_2$ exhibited an extraordinarily high capacity from abnormal lithium storage sites.[29] According to Shon *et al.*, upon lithiation, lithium ions firstly inserted into the lattice of $MoO_2$ lead to the formation of a lithium-intercalated $MoO_2$ crystalline phase up to $Li_{0.98}MoO_2$. Next, more lithium ions were stored at the interface between the $Li_xMoO_2$ domains as a metallic state, resulting in the formation of amorphous metallic lithium clusters.[29] This reaction process created no other crystalline phases, except for those of $MoO_2$ and $Li_xMoO_2$. This reaction pathway matched the *ex situ* XRD patterns (Fig. 4b). Reverse phase transition was observed upon subsequent discharge,[53,54] revealing that the 2D-$SiO_x$/0D-$MoO_2$ nanocomposites underwent highly reversible phase transition during lithiation and delithiation, explaining the stable cycling performance of the 2D-$SiO_x$/0D-$MoO_2$ nanocomposite electrode. The presented exceptional reaction pathways of 0D-$MoO_2$ particles played an important role in improving the lithium storage properties of the 2D-$SiO_x$ nanosheets without degrading the superior physicochemical properties of 2D-$SiO_x$ nanosheets.

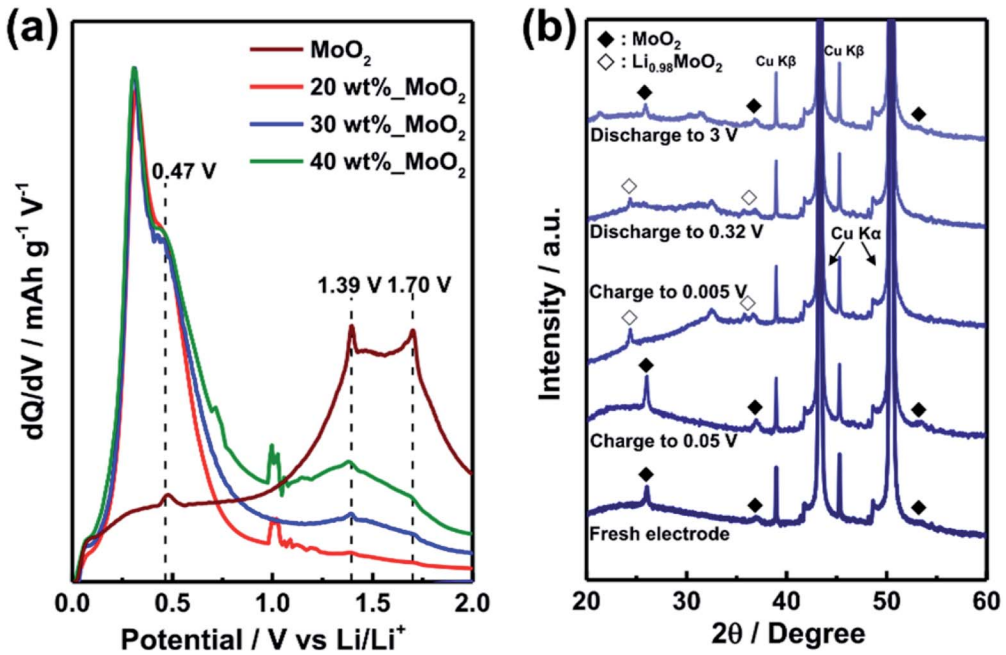


Fig. 4 (a) Differential capacity plots of the first discharge for the 2D-$SiO_x$/0D-$MoO_2$ nanocomposites with different amounts of $MoO_2$. (b) *Ex situ* XRD patterns of the 2D-$SiO_x$/0D-$MoO_2$ nanocomposites electrodes for the first cycle.

## Conclusions

We demonstrated a rational design for chemically anchored 2D-$SiO_x$/0D-$MoO_2$ nanocomposites using a Mo–O–Si bond through a carbothermic reduction route with urea as a reducing agent. Introduction of 0D-$MoO_2$ nanoparticles helped compensate for the shortcomings of 2D-$SiO_x$ nanosheets in terms of reversible capacity and initial coulombic efficiency without sacrificing cycling performance. Such improvements can be achieved through a synergistic effect of the unique properties of the 2D-$SiO_x$ nanosheets (favorable microstructures and dimensional stability) and the 0D-$MoO_2$ nanoparticles (abnormal lithium storage sites and highly reversible phase transition). The results showed that our material approach to enhance lithium storage properties by creating bonds with the 0D-$MoO_2$ nanoparticles at the surface of 2D-$SiO_x$ nanosheets can maximize the unique physicochemical properties of 2D nanomaterial-based nanocomposites for next-generation electrochemical energy storage application.

## Conflicts of interest

There are no conflicts to declare.

## Acknowledgements

This work was supported by the Samsung Research Funding Center for Future Technology (SRFC-MA1401-52).

## Notes and references

1 B. Scrosati, *Nature*, 2011, **473**, 448–449.
2 J. B. Goodenough and K. S. Park, *J. Am. Chem. Soc.*, 2013, **135**, 1167–1176.
3 E. C. Evarts, *Nature*, 2015, **526**, S93–S95.
4 N. Nitta, F. X. Wu, J. T. Lee and G. Yushin, *Mater. Today*, 2015, **18**, 252–264.
5 J. Lu, Z. H. Chen, Z. F. Ma, F. Pan, L. A. Curtiss and K. Amine, *Nat. Nanotechnol.*, 2016, **11**, 1031–1038.
6 V. Etacheri, R. Marom, R. Elazari, G. Salitra and D. Aurbach, *Energy Environ. Sci.*, 2011, **4**, 3243–3262.
7 J. W. Choi and D. Aurbach, *Nat. Rev. Mater.*, 2016, **1**, 16013.
8 F. Y. Cheng, J. Liang, Z. L. Tao and J. Chen, *Adv. Mater.*, 2011, **23**, 1695–1715.
9 G. Jeong, Y. U. Kim, H. Kim, Y. J. Kim and H. J. Sohn, *Energy Environ. Sci.*, 2011, **4**, 1986–2002.
10 C. M. Park, J. H. Kim, H. Kim and H. J. Sohn, *Chem. Soc. Rev.*, 2010, **39**, 3115–3141.
11 S. M. Hwang, Y. G. Lim, J. G. Kim, Y. U. Heo, J. H. Lim, Y. Yamauchi, M. S. Park, Y. J. Kim, S. X. Dou and J. H. Kim, *Nano Energy*, 2014, **10**, 53–62.
12 M. Pramanik, M. Imura, J. J. Lin, J. Kim, J. H. Kim and Y. Yamauchi, *Chem. Commun.*, 2015, **51**, 13806–13809.
13 D. Bresser, S. Passerini and B. Scrosati, *Energy Environ. Sci.*, 2016, **9**, 3348–3367.
14 T. D. Hatchard and J. R. Dahn, *J. Electrochem. Soc.*, 2004, **151**, A838–A842.
15 U. Kasavajjula, C. S. Wang and A. J. Appleby, *J. Power Sources*, 2007, **163**, 1003–1039.
16 M. N. Obrovac and L. J. Krause, *J. Electrochem. Soc.*, 2007, **154**, A103–A108.
17 R. A. Huggins and W. D. Nix, *Ionics*, 2000, **6**, 57–63.
18 L. Y. Beaulieu, K. W. Eberman, R. L. Turner, L. J. Krause and J. R. Dahn, *Electrochem. Solid-State Lett.*, 2001, **4**, A137–A140.
19 A. Magasinski, P. Dixon, B. Hertzberg, A. Kvit, J. Ayala and G. Yushin, *Nat. Mater.*, 2010, **9**, 353–358.
20 W. J. Zhang, *J. Power Sources*, 2011, **196**, 13–24.
21 H. Wu and Y. Cui, *Nano Today*, 2012, **7**, 414–429.
22 R. Yi, F. Dai, M. L. Gordin, S. R. Chen and D. H. Wang, *Adv. Energy Mater.*, 2013, **3**, 295–300.
23 M. S. Park, E. Park, J. Lee, G. Jeong, K. J. Kim, J. H. Kim, Y. J. Kim and H. Kim, *ACS Appl. Mater. Interfaces*, 2014, **6**, 9608–9613.
24 H. Yoo, E. Park, J. Bae, J. Lee, D. J. Chung, Y. N. Jo, M. S. Park, J. H. Kim, S. X. Dou, Y. J. Kim and H. Kim, *Sci. Rep.*, 2018, **8**, 6904.
25 M. Zheng, D. Qiu, B. Zhao, L. Ma, X. Wang, Z. Lin, L. Pan, Y. Zheng and Y. Shi, *RSC Adv.*, 2013, **3**, 699–703.
26 Z. Jian, B. Zhao, P. Liu, F. Li, M. Zheng, M. Chen, Y. Shi and H. Zhou, *Chem. Commun.*, 2014, **50**, 1215–1217.
27 J. F. Ni, Y. Zhao, L. Li and L. Q. Mai, *Nano Energy*, 2015, **11**, 129–135.
28 A. Kim, E. Park, H. Lee and H. Kim, *J. Alloys Compd.*, 2016, **681**, 301–306.
29 J. K. Shon, H. S. Lee, G. O. Park, J. Yoon, E. Park, G. S. Park, S. S. Kong, M. Jin, J. M. Choi, H. Chang, S. Doo, J. M. Kim, W. S. Yoon, C. Pak, H. Kim and G. D. Stucky, *Nat. Commun.*, 2016, **7**, 11049.
30 A. M. Chu, M. L. Qin, R. Ud-din, B. R. Jia, H. F. Lu and X. H. Qu, *J. Alloys Compd.*, 2012, **530**, 144–151.
31 H. Takezawa, K. Iwamoto, S. Ito and H. Yoshizawa, *J. Power Sources*, 2013, **244**, 149–157.
32 E. Park, H. Yoo, J. Lee, M. S. Park, Y. J. Kim and H. Kim, *ACS Nano*, 2015, **9**, 7690–7696.
33 E. Park, M. S. Park, J. Lee, K. J. Kim, G. Jeong, J. H. Kim, Y. J. Kim and H. Kim, *ChemSusChem*, 2015, **8**, 688–694.
34 J. Bae, D. S. Kim, H. Yoo, E. Park, Y. G. Lim, M. S. Park, Y. J. Kim and H. Kim, *ACS Appl. Mater. Interfaces*, 2016, **8**, 4541–4547.
35 L. Zheng, Y. Xu, D. Jin and Y. Xie, *J. Mater. Chem.*, 2010, **20**, 7135–7143.
36 X. L. Liu, D. Wu, W. X. Ji and W. H. Hou, *J. Mater. Chem. A*, 2015, **3**, 968–972.
37 P. A. Spevack and N. S. Mcintyre, *J. Phys. Chem.*, 1992, **96**, 9029–9035.
38 N. Tomozeiu, *Appl. Surf. Sci.*, 2006, **253**, 376–380.
39 H. Guo, R. Mao, X. J. Yang and J. Chen, *Electrochim. Acta*, 2012, **74**, 271–274.
40 M. R. S. Kebria, M. Jahanshahi and A. Rahimpour, *Desalination*, 2015, **367**, 255–264.
41 H. Sanaeishoar, M. Sabbaghan and F. Mohave, *Microporous Mesoporous Mater.*, 2015, **217**, 219–224.
42 K. Eda, *J. Solid State Chem.*, 1991, **95**, 64–73.

 

43 M. M. Mohamed and G. M. S. Elshafei, *Spectrochim. Acta, Part A*, 1995, **51**, 1525–1531.
44 B. C. Yu, Y. Hwa, J. H. Kim and H. J. Sohn, *Electrochim. Acta*, 2014, **117**, 426–430.
45 E. Zhou, C. G. Wang, M. H. Shao, X. L. Deng and X. J. Xu, *Ceram. Int.*, 2017, **43**, 760–765.
46 M. Fenech, S. Lim, J. Cheung and N. Sharma, *Phys. Chem. Chem. Phys.*, 2019, **21**, 25779–25787.
47 B. K. Guo, X. P. Fang, B. Li, Y. F. Shi, C. Y. Ouyang, Y. S. Hu, Z. X. Wang, G. D. Stucky and L. Q. Chen, *Chem. Mater.*, 2012, **24**, 457–463.
48 B. C. Yu, Y. Hwa, C. M. Park and H. J. Sohn, *J. Mater. Chem. A*, 2013, **1**, 4820–4825.
49 J. Woo and S. H. Baek, *RSC Adv.*, 2017, **7**, 4501–4509.
50 K. Palanisamy, Y. Kim, H. Kim, J. M. Kim and W. S. Yoon, *J. Power Sources*, 2015, **275**, 351–361.
51 J. B. Boland, A. Harvey, R. Y. Tian, D. Hanlon, V. Vega-Mayoral, B. Szydlowska, A. Griffin, T. Stimpel-Lindner, S. Jaskaniec, V. Nicolosi, G. Duesberg and J. N. Coleman, *Nanoscale Adv.*, 2019, **1**, 1560–1570.
52 Q. Xie and D. L. Peng, in *Advanced Battery Materials*, ed. C. Sun, Scrivener Publishing, Massachusetts, 1st edn, 2019, ch. 3, pp. 185–189.
53 J. R. Dahn and W. R. Mckinnon, *Solid State Ionics*, 1987, **23**, 1–7.
54 K. Ben-Kamel, N. Amdouni, H. Groult, A. Mauger, K. Zaghib and C. M. Julien, *J. Power Sources*, 2012, **202**, 314–321.